Circular-Photon-Drag-Effect-Induced Elliptically Polarized Terahertz Emission from Vertically Grown Graphene

Lipeng Zhu,[1,2] Zehan Yao,[1] Yuanyuan Huang,[1] Chuan He,[1] Baogang Quan,[3] Junjie Li,[3] Changzhi Gu,[3] Xinlong Xu,[1,*] and Zhaoyu Ren[1]

[1] *Shaanxi Joint Lab of Graphene, International Collaborative Center on Photoelectric Technology and Nano Functional Materials, Institute of Photonics & Photon-Technology, Northwest University, Xi'an 710069, China*
[2] *School of Electronic Engineering, Xi'an University of Posts and Telecommunications, Xi'an 710121, China*
[3] *Beijing National Laboratory for Condensed Matter Physics, and Institute of Physics, Chinese Academy of Sciences, Beijing 100190, China*

(Received 4 June 2019; revised manuscript received 10 September 2019; published 28 October 2019)

Circular photon drag effect (CPDE) is important for helicity-dependent optoelectronic emitters and detectors yet is less studied in graphene due to the relatively weak light-matter interaction and is submerged by other nonlinear optical effects. We give experimental evidence of CPDE in vertically grown graphene (VGG) by terahertz (THz) emission spectroscopy. The emitted THz polarization states can be tuned to linear, left-handed, and right-handed elliptical polarizations by changing the helicity of the pump laser. Polarity reversal of the THz time-domain signal occurs with the opposite helicity of pump laser excitation due to the CPDE. Theory analysis suggests that both the linear photon drag effect and CPDE-induced transient photocurrents contribute to the THz emission from which the contribution weight of CPDE can be tuned by different elliptical states of the excitation light. The photon-helicity-dependent THz emission from VGG based on CPDE offers an alternative thought of graphene-based polarization sensitive THz sources for chiral analysis in the THz field.

DOI: 10.1103/PhysRevApplied.12.044063

I. INTRODUCTION

Even though Poynting realized light can carry spin angular momentum (SAM) in 1909, Beth did not demonstrate that the SAM can transfer to the dipoles in a quartz waveplate (namely, polarization by the circular light in classic physics) to produce a torque effect until 1936 [1]. However, the transfer of SAM from photons to the charges (free electrons or holes) to form a photocurrent without a bias came into reality in 2006 in a two-dimensional electron gas in GaAs quantum wells [2]. This so-called circular photon drag effect (CPDE) is a second-order nonlinear optical effect, which is usually mixed with other optical effects such as circular photogalvanic effect (CPGE) and spin photogalvanic effect (SPGE) originating from both band structure specifics and contact in a low-dimensional system [3]. The CPGE originates from either the asymmetrical momentum distribution of photoexcited carriers or the different spin relaxation of optically oriented carriers [4]. The SPGE results are from the spin splitting into spin-up and spin-down subbands, which shift along k space and result in nonequilibrium spin distribution for the photocurrent without a bias [5]. The CPGE and SPGE are usually allowed in noncentrosymmetric materials, while CPDE can exist in any kind of symmetric material as CPDE is also related to the wave vector.

Originally, CPDE-induced electric currents could be measured with a dc electrical method by electrode contact [6]. However, contact could break the symmetry and introduce some parasitic interface effects such as a built-in electric effect and a photothermoelectric effect at the interface [7]. Considering the fact that CPDE-induced time-dependent photocurrents driven by a femtosecond (fs) laser can emit picosecond terahertz (THz) electromagnetic radiation, THz emission spectroscopy is becoming a promising method to detect transient photocurrents without electrodes and with more information such as polarity, amplitude, and phase. This method was first suggested to detect the ballistic photocurrent in graphene by Sun *et al.* [8]. In particular, THz emission spectroscopy can be used to probe the helicity-dependent ultrafast photocurrents in CPGE in topological insulators [9,10] and other advanced nanomaterials [11]. However, there is no report on the CPDE with THz emission spectroscopy as the CPDE is under the background of CPGE and SPGE.

Unlike other low-dimensional materials, graphene with a D_{6h} symmetry point group can restrain the photon-helicity-dependent photocurrents from CPGE and SPGE,

---

[*] xlxuphy@nwu.edu.cn

which affords a model system to resolve the helicity-dependent THz emission from CPDE. In recent years, the linear photon drag effect (LPDE) by linear polarized light excitation has been observed in monolayer graphene, which can distinguish the LPDE from the linear photogalvanic effect (LPGE) as the symmetry forbids the LPGE due to the unique properties of graphene, such as strong electron-phonon coupling, higher momentum transfer rate, and shorter momentum relaxation time [12]. These properties make LPDE easier to observe under excitation by an 800-nm (1.55 eV) fs laser [12–15]. However, limited by the low interaction of graphene and light, the THz emission from graphene is relatively small, which prevents further CPDE observation by THz emission spectroscopy. Recently, we have shown 10 times enhanced THz emission in amplitude from vertically grown graphene (VGG) instead of planar growth graphene due to a special light trap to enhance the light-graphene interaction [16]. This enhancement allows us a thorough understanding of the underlying transient carrier dynamics in CPDE involving the helicity-dependent states.

The helicity-dependent THz emission from VGG has been studied systematically in this work, which agrees well with the CPDE theory. The polarization trajectory of the THz signals demonstrates elliptical polarization THz emission, which can be controlled by the pump polarization states. The CPDE-based helicity-dependent transient photocurrents in VGG can be used as an elliptically polarized THz emitter. Control of elliptically polarized THz emission is not only technically difficult, but scientifically useful in chiral analysis with THz electromagnetic waves [17,18].

II. EXPERIMENT

A. Sample characterization

The VGG sample is synthesized by a microwave plasma-enhanced chemical vapor deposition (MPCVD) method [16]. The scanning electron microscopy (SEM, Helios 600i, FEI) image of the VGG is shown in Fig. 1(a), in which the flowerlike graphene flakes with many sharp edges grow vertically on the fused quartz substrate.

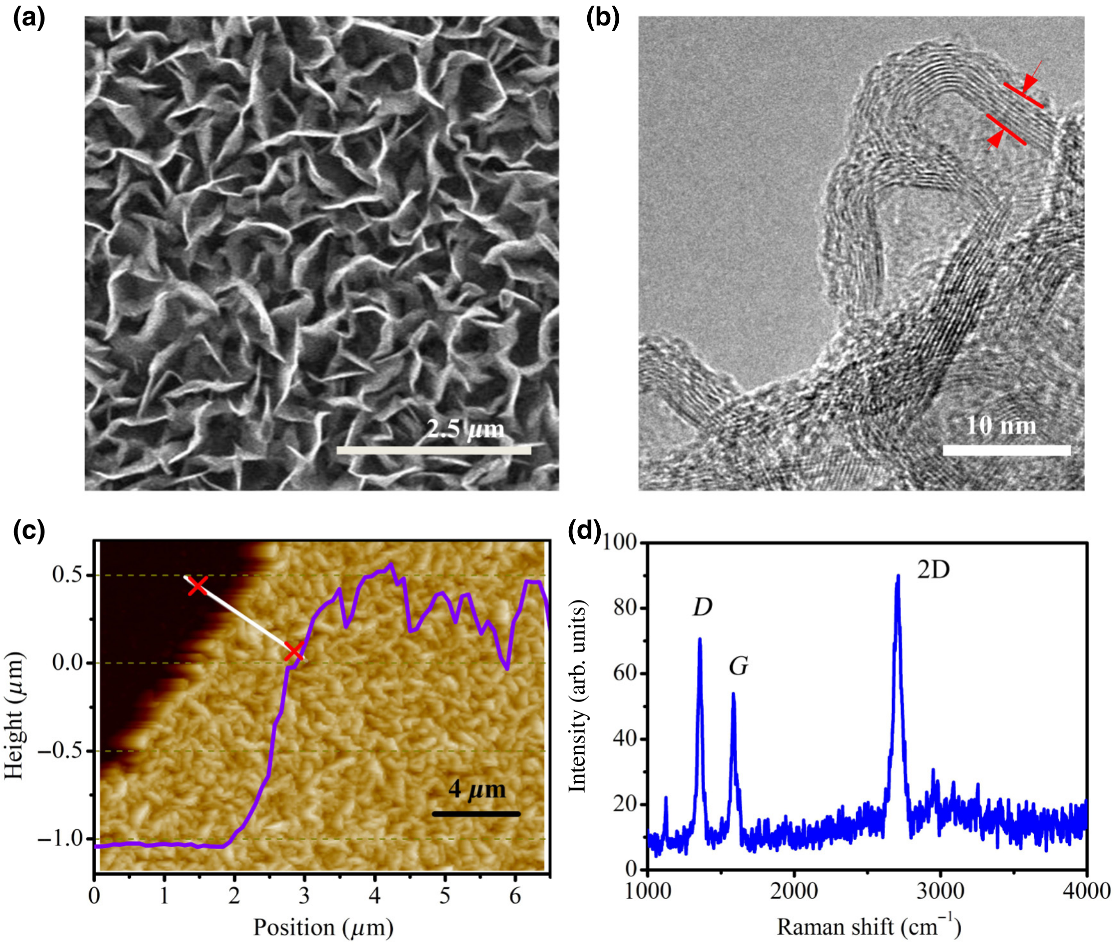

FIG. 1. (a) SEM image of VGG sample. (b) High-resolution TEM image of VGG. (c) AFM image of VGG with a height mode. (d) Raman spectrum of VGG with the excitation wavelength of 514 nm.

Transmission electron microscopy (TEM, Tecnai G2 F20, FEI) is also utilized to characterize the graphene layer number in Fig. 1(b). We can observe that the layer number is approximately 7–8. An atomic force microscope (AFM, Dimension Icon, Veeco) is also used to map the boundary of the sample and determine the thickness of the sample as shown in Fig. 1(c). The thickness is approximately 1.5 μm as shown in the insert of Fig. 1(c) along the straight white line. The sample is also identified by Raman spectroscopy excited by a 514-nm laser. As shown in Fig. 1(d), there are three characteristic peaks at 1355.93, 1584.71, and 2711.25 cm^{-1} that originate from the first-order scattering defect band (D band), in-plane vibration mode (G band), and combination mode (2D band) [19], respectively.

B. THz experimental setup

The THz emission spectroscopy setup is illustrated in Fig. 2(a) as described in our previous work [16]. A Ti:sapphire mode-locked fs laser regenerated amplifier (Spectra Physics, 800 nm, 1 kHz, 35 fs) is divided into the pump and the probe beams with Pump 1 for the transmission configuration and Pump 2 for the reflection configuration. The pump intensity is 50 mW and the pump beam is loosely focused onto the sample (spot diameter of 3 mm). A quarter-wave plate (QWP) is used to obtain the different elliptical polarization states of the pump beam via rotating the QWP polarization angle ϕ. The angle ϕ is an included angle between the fast axis of the QWP and the electric vector of the linearly polarized pump beam. The emitted THz radiation can be collected and detected by a ZnTe ⟨110⟩ crystal. Figure 2(b) shows the definition of the crystal coordinates xyz and laboratory coordinates XYZ. The plane xy is the graphene sample plane and axis z is perpendicular to the sample plane. The plane XZ is the pump light incident plane and angle θ is the incident angle. In a nonlinear optical process, the incident angle of the pump beam and reflected and transmitted THz field wave vectors satisfy the generalized Snell's law [20,21]. The electric vectors of THz p and s polarization components are denoted as E_{THz}^{p} and E_{THz}^{s} in Fig. 2(b), which can be analyzed by two wire-grid polarizers (WGP) [12]. Considering the arrangement of VGG on the substrate, we define a rotation angle γ from axis y to axis Y.

III. RESULT AND DISCUSSION

A. CPDE of VGG in theory

As the elliptical and circular polarization beams both have transverse momentum and SAM, the photocurrents in graphene excited by elliptical or circular polarization light can be expressed as [22]

$$j_{\lambda} = T_{\lambda\mu\nu\eta} q_{\mu} \frac{e_{\nu}^{*} e_{\eta} + e_{\nu} e_{\eta}^{*}}{2} I + \tilde{T}_{\lambda\mu\nu} q_{\mu} P_{\mathrm{circ}} \hat{e}_{\nu} I, \qquad (1)$$

where q is the wave vector of light. Letter e is the unit vector of the light electric vector and $\hat{e}$ is the unit vector along the direction of light propagation. I is the light intensity and $P_{\mathrm{circ}} = \sin 2\phi$ is the helicity of the pump light with the angle ϕ defined in Fig. 2(b) ($P_{\mathrm{circ}} = 1$ for the left-handed circular polarization, while $P_{\mathrm{circ}} = -1$ for the right-handed circular polarization). The fourth-rank tensor $T_{\lambda\mu\nu\eta}$ describes the LPDE, while the third-rank pseudotensor $\tilde{T}_{\lambda\mu\nu}$ describes CPDE. From Eq. (1), the CPDE-induced photocurrent is sensitive to the helicity and changes its sign with the reversal of the photon helicity of the pump light (for example, P_{circ} from $+1$ to -1).

As the graphene vertically grows on the substrate, the VGG can be thought as free-standing multilayer graphene flakes without a substrate. The symmetry point group of multilayer graphene is dependent on the two stacking types such as the Bernal stacking (ABAB…) described by D_{3d} for the even layer numbers, D_{3h} for the odd layer numbers [23,24], and rhombohedral stacking (ABCABC…)

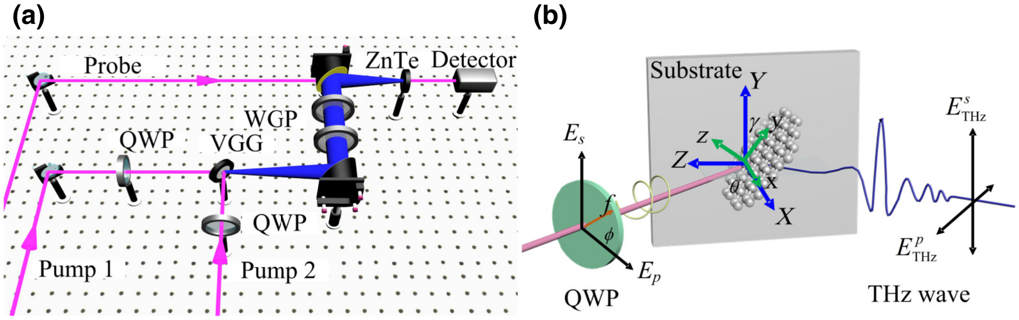

FIG. 2. (a) A typical THz emission spectroscopy experimental setup. Pump 1 and Pump 2 are the pump beams for transmission and reflection configurations, respectively. A QWP is used to change the light helicity of the pump beam. Two WGP are used to analyze the THz wave polarization states. (b) Definition of the crystal coordinates xyz (green, with z perpendicular to the graphene surface) and laboratory coordinates XYZ (blue, with X perpendicular to the substrate). Axis f is the fast axis of the QWP. ϕ and θ are polarization angles of the QWP and incident angle, respectively. E_{THz}^{p} and E_{THz}^{s} are p polarization and s polarization of the THz wave components.

described by the D_{3d} symmetry point group [24]. In general, the photocurrent in crystal coordinate xyz after considering the above possible symmetry point can be expressed as follows: [details in Eqs. (A1)–(A9) and Table I in Appendix A]:

$$j_x = T_1 q_x \frac{|E_x|^2 + |E_y|^2}{2} + T_2 q_x \frac{|E_x|^2 - |E_y|^2}{2} + \tilde{T}_{xxy} q_x E_y^2 P_{\text{circ}} - L(E_x E_y^* + E_y E_x^*), \tag{2}$$

$$j_y = T_2 q_x \frac{E_x E_y^* + E_x^* E_y}{2} - \tilde{T}_1 q_x P_{\text{circ}} \hat{e}_z (|E_x|^2 + |E_y|^2) + \tilde{T}_{yxx} q_x E_x^2 P_{\text{circ}} + L(E_y^2 - E_x^2), \tag{3}$$

where T_1, T_2, and $\tilde{T}_1$ are related to the nonlinear tensor elements from $T_{\lambda\mu\nu\eta}$ and $\tilde{T}_{\lambda\mu\nu}$ in Eq. (1), simplified due to the D_{3d} symmetry point group. From Eqs. (2) and (3), the j_x photocurrent along the x axis and j_y along the y axis in Fig. 2(b) come from the combination of LPDE and CPDE. Both D_{3d} and D_{3h} symmetry point groups can exclude the CPGE. In microscopic theory, the presence or absence of SAM in photons is a symbol to distinguish CPDE from LPDE. Compared with linear polarization excitation, the elliptical or circular polarization excitation has the following special features: (1) Both transverse momentum and SAM of photons have been transferred to carriers. (2) The CPDE-induced photocurrents are sensitive to the helicity of pump light and reverse the photocurrent's direction (THz signal polarity) when switching the helicity from left-handed circular (LC) to right-handed circular (RC) polarization and vice versa.

For ease of comparation with the experimental results, we rewrite Eqs. (2) and (3) with the QWP polarization angle ϕ and incident angle θ. The projection of the electric vector in the graphene plane can be expressed as [details in Eqs. (B1)–(B3) in Appendix B]

$$\begin{bmatrix} E_x \\ E_y \end{bmatrix} = E \begin{bmatrix} \sin\theta(\cos^2\phi + i\sin^2\phi) \\ \cos\gamma \left(\frac{1}{2} - \frac{i}{2}\right) \sin 2\phi \end{bmatrix}. \tag{4}$$

Therefore, the photocurrents in the graphene plane can be rewritten as [details in Eqs. (B4)–(B8) in Appendix B]

$$\begin{aligned} j_x = &-\frac{E^2}{8} k \cos\theta (T_1 + T_2) \sin^2\theta \{3 + \cos 4\phi\} \\ &- \frac{E^2}{4} k \cos\theta (T_1 - T_2) \cos^2\gamma \sin^2 2\phi \\ &- \tilde{T}_{xxy} \frac{1}{2} E^2 k \cos\theta \sin^3 2\phi \cos^2\gamma \\ &- L E^2 \frac{1}{4} \sin\theta \cos\gamma \sin 4\phi, \end{aligned} \tag{5}$$

$$\begin{aligned} j_y = &-T_2 E^2 \frac{1}{8} k \cos\theta \cos\gamma \sin\theta \sin 4\phi \\ &- \tilde{T}_1 E^2 k \cos\theta \sin\theta \sin 2\phi \\ &\times \left[\frac{1}{4}\sin^2\theta(3 + \cos 4\phi) + \frac{1}{2}\cos^2\gamma \sin^2 2\phi\right] \\ &- \tilde{T}_{yxx} k \cos\theta E^2 \frac{1}{4} \sin^2\theta (3 + \cos 4\phi) \sin 2\phi \\ &- L E^2 \left[\frac{1}{4}\sin^2\theta(3 + \cos 4\phi) + \frac{1}{2}\cos^2\gamma \sin^2 2\phi\right], \end{aligned} \tag{6}$$

where $k = \omega/c$ is the wave vector. In terms of THz detection of the whole VGG sample, transformation from crystal coordinates xyz to laboratory coordinates XYZ in Fig. 2(b) should be considered. The projection of photocurrents in XYZ coordinates can be further expressed as Eqs. (B9)–(B11) (Appendix B) by the coordinate transformation. Considering the dipole radiation theory, the detected THz components can be written as [details in (B12) and (B13) in Appendix B]

$$\begin{aligned} E_{\text{THz}}^p &\propto t_p \left(\sin\theta_{\text{in}} \frac{\partial j_X}{\partial t} + \cos\theta_{\text{in}} \frac{\partial j_Z}{\partial t}\right) \\ &\propto L_1 \cos 4\phi + M \sin^2 2\phi + C_1 \sin 2\phi \cos 4\phi \\ &\quad + C_2 \sin 2\phi + C_3 \sin^3 2\phi + D, \end{aligned} \tag{7}$$

$$\begin{aligned} E_{\text{THz}}^s \propto t_s \frac{\partial j_Y}{\partial t} &\propto L_2 \sin 4\phi + C_4 \sin 2\phi \\ &+ C_5 \sin 2\phi \cos 4\phi + C_6 \sin^2 2\phi, \end{aligned} \tag{8}$$

where t_p and t_s are the transmission coefficients for THz p and s polarizations at the VGG-air interface. $\theta_{\text{in}} = \arcsin(\sqrt{\varepsilon_1/\varepsilon_2} \sin\theta)$ is the radiation angle in sample VGG for the THz wave. The coefficients L_1 and L_2 are related to $T_1 + T_2$ and T_2. C_1 and C_2 are related to $\tilde{T}_1 + \tilde{T}_{yxx}$. C_3, C_4, C_5, and C_6 are related to $\tilde{T}_{xxy}$, $\tilde{T}_1 + \tilde{T}_{yxx}$, $\tilde{T}_1 + \tilde{T}_{yxx}$, and $\tilde{T}_1$, respectively. M is related to $\tilde{T}_1$ and $T_1 + T_2$. D is a constant and is related to $T_1 + T_2$. Here, we ignored the L terms caused by the D_{3h} point group in Eqs. (5) and (6) and the reason will be discussed in the next part. According to Eqs. (7) and (8), the contributions of LPDE and CPDE can be determined by fitting the helicity-dependent THz emission, which can be readily obtained in both transmission configuration and reflection configuration.

B. THz emission in transmission configuration

In the experiment, both the incident angle and polarization angle can change the amplitude and polarity of the THz radiation from VGG. THz time-domain signals of p and s polarizations with an incident angle of $\theta = -25^\circ$ are shown in Figs. 3(a) and 3(b), respectively, in which

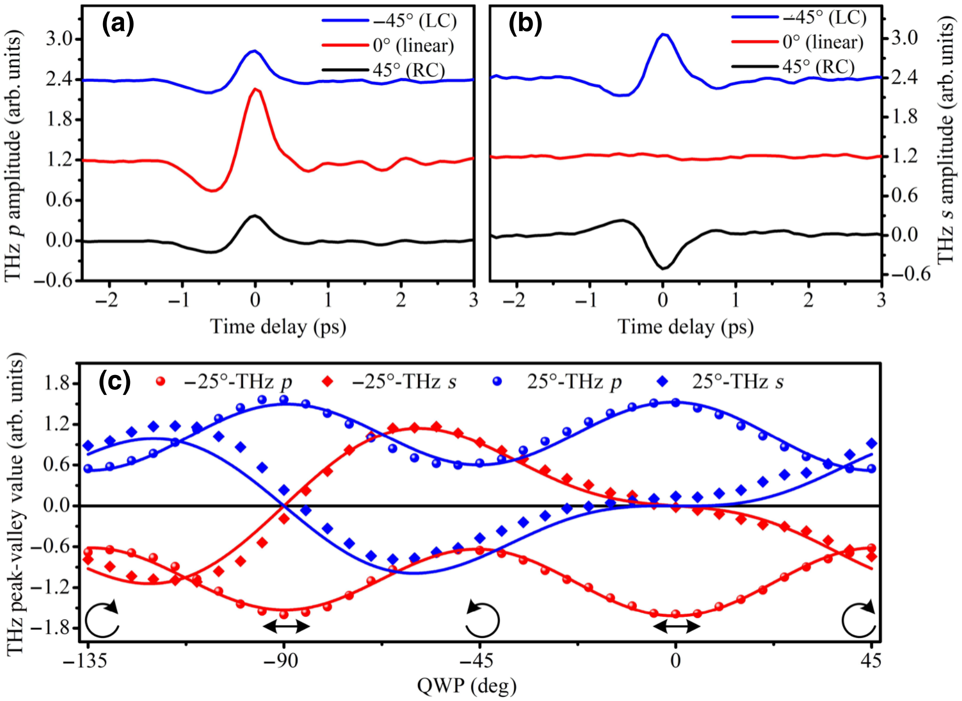

FIG. 3. (a) THz time-domain signals of *p* polarization component and (b) *s* polarization component with QWP angles −45°, 45°, and 0° corresponding to LC, RC polarization and linear polarization of the pump light at the incident angles of −25°, respectively. (c) The dependence of THz peak-valley value on the QWP angles. The polarization states of the pump are shown at the bottom of the figure.

the QWP polarization angles are set to −45°, 0°, and 45° corresponding to LC, linear, and RC polarization states. In terms of THz *p* components, the THz driven by LC- or RC-polarized pulses' excitation has equal amplitudes and similar polarity. The equal THz amplitudes means the photocurrents contributing to THz *p* polarization are equal, $j\,(\phi = 45^{\circ}) = j\,(\phi = -45^{\circ})$, which requires that C_1, C_2, and C_3 are zero. The condition that the THz amplitude under the linear polarization excitation is nearly two times larger than that under LC or RC excitation results in the relationship $D = 3L_1 - M$. In terms of THz *s* components, the time-domain signals have equal amplitudes but with an opposite polarity driven by LC and RC polarized fs pulses. In order to satisfy the condition $j_Y(\phi = 45^{\circ}) = -j_Y(\phi = -45^{\circ})$ as shown in Fig. 3(b), the last L related terms in Eqs. (5) and (6) must vanish and C_6 is zero. Therefore, Eqs. (7) and (8) can be further simplified as follows:

$$E^{p}_{\mathrm{THz}} \propto t_p \left(\sin\theta_{\mathrm{in}} \frac{\partial j_X}{\partial t} + \cos\theta_{\mathrm{in}} \frac{\partial j_Z}{\partial t} \right)$$
$$\propto L_1 \cos 4\phi + M \sin^2 2\phi + 3L_1 - M, \tag{9}$$

$$E^{s}_{\mathrm{THz}} \propto t_s \frac{\partial j_Y}{\partial t} \propto L_2 \sin 4\phi + C_4 \sin 2\phi + C_5 \sin 2\phi \cos 4\phi. \tag{10}$$

In particular, when excited by LC or RC polarized pulses, Eqs. (9) and (10) show that THz *p* polarization components come from the contribution of LPDE and CPDE, while the *s* polarization components result from CPDE. Therefore, VGG offers a platform to investigate pure CPDE.

The spectra of Figs. 3(a) and 3(b) in the frequency domain can be acquired by fast Fourier transformation (Fig. 6 and Appendix C), which shows that the THz bandwidths are up to 3 THz no matter what the polarization states of the pump beam. In theory, the bandwidth of graphene-based THz radiation can be up to 60 THz [14], which is limited by the detection crystal.

To further investigate the dependence of THz amplitude on the pump polarization states, Fig. 3(c) shows that the THz peak-valley values (the value difference between the peak and the valley of the THz time-domain signal) for both *p* and *s* polarization components change with the QWP polarization angle ϕ in the transmission configuration with an incident angle $\theta = \pm 25^{\circ}$. The negative peak-valley value means signal polarity reversal. Two features should be noted: (1) the peak-valley values change their amplitudes periodically with the QWP angle, for example, a $\cos 4\phi$ style variation for THz *p* components and a quasi-$\sin 2\phi$ style for *s* components at an incident angle of either 25° or −25°. (2) The polarity reversal occurs for the *s* components when the pump state switches from LC to RC polarization. This THz polarity reversal behavior has also been found in topological insulator materials, such as $\mathrm{Bi_2Se_3}$ [10] and $\mathrm{Sb_2Te_3}$ [25] as explained by CPDE or CPGE. In general, both the LPDE and CPDE contribute to the THz emission from VGG driven by elliptical polarized light, which can be fitted well with Eqs. (9) and (10) as shown in Fig. 3(c) (the solid lines). Compared with the maximum THz peak-valley value of 1.62, the amplitude of CPDE related M is only 0.32 for THz p components, which is submerged by the LPDE. However, for the s component, the fitted coefficient C_4 is up to 0.8, which gives evidence that CPDE dominates the THz s polarization. The contribution of CPDE varies for different QWP angles. Moreover, this helicity sensitive THz emission from VGG makes it easier to control by changing the polarization of the pump light.

The THz radiation only appears at oblique incidence and reverses its polarity when switched to the opposite incident angle as shown in Fig. 7 (Appendix D). This phenomenon was also observed in graphene under circular THz wave irradiation, which is caused by the dynamic Hall effect [26]. The polarity reversal with the incident angle can be explained as both LPDE and CPDE are dependent on the wave vector projection q_x and $\hat{e}_z$ in the graphene plane in Eqs. (2) and (3) with the opposite incident angle for the opposite wave vectors. In microscopic description [14], the distribution of photoinduced nonthermal carriers (electrons and holes) is asymmetric in momentum space at oblique incidence, which can cause a net transient current. Previous works [3,26,27] have studied the helicity-dependent electrical current from graphene excited with photon energy $\hbar\omega$ lower than the Fermi level E_F (100–300 meV) of graphene. This is in the classical region with the intraband transition, which can be described by the Boltzmann function in a microscopic theory [28]. However, in our experiments, the excited photon energy satisfies $\hbar\omega \gg 2E_F$, which is in the quantum region where interband transition is allowed while the transition below Fermi level is forbidden, which leads to a sharp momentum distribution [29].

To investigate the dependence of THz polarization states on the pump helicity, we reconstruct the electric trajectories of the emitted THz pulses by composing THz p and s polarization components as shown in Fig. 4 with the incident angles of ±25°. The bottom (red dotted line)

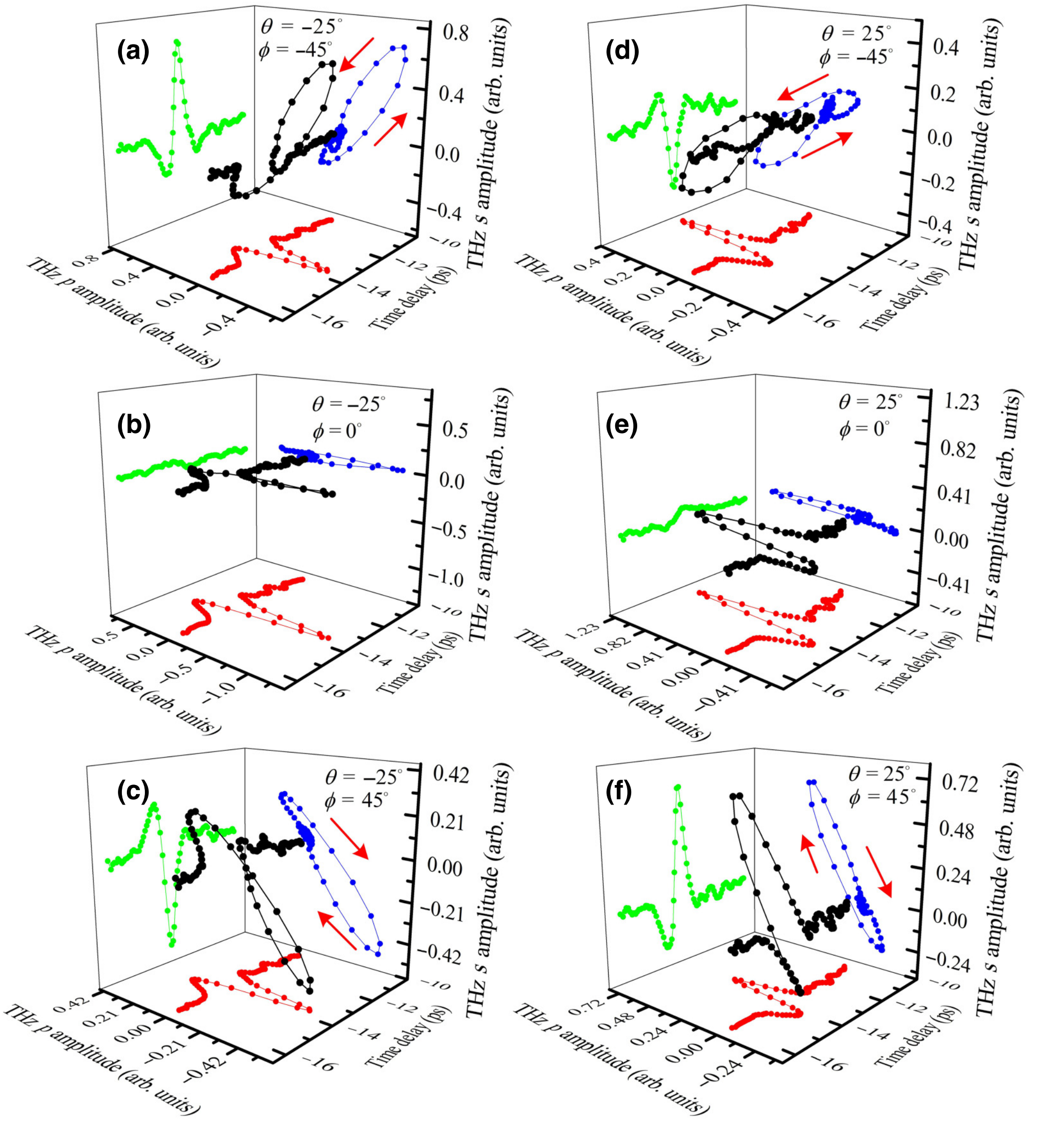

FIG. 4. THz polarization reconstruction in a transmission configuration with two opposite incident angles. (a)–(c) are trajectories of the emitted THz polarization states portrayed with the QWP angles of −45° (LC), 0° (linear), and 45° (RC) at the incident angle of −25°, respectively. (d)–(f) are the counterparts with the incident angle of 25°. The blue dotted lines on the right panel represent the THz polarization states and the red arrows mark the helicity direction of the THz electric vectors.

and the back panel (green dotted line) are the time-domain waveforms of the THz p and s components, respectively. The central black dotted line shows the sum of the THz waveforms, while the right panel blue dotted line represents the THz electric vector projection along the THz propagation direction. The red arrows clearly mark the helicity direction of the THz electric field vector. It is shown that a linearly polarized excitation [Figs. 4(b) and 4(e)] leads to almost linearly polarized THz radiation, while left-handed [Figs. 4(a) and 4(d)] and right-handed [Figs. 4(c) and 4(f)] elliptically polarized THz radiation states can be acquired under LC and RC polarized pump excitations, respectively. The results show that the sign of the incident angle has no effect on the THz polarization states. To quantitatively clarify the elliptical polarization states, we fit the electric vector projection using the least squares method [30] as shown in Fig. 8 (Appendix E)to get the ellipticity and inclined angle of the ellipse in Table II (Appendix E). Here, the ellipticity is defined as $e = b/a$, where a and b are the lengths of the long and short axes of the ellipse, respectively. The inclined angle is the angle between the direction of E^{p}_{THz} and the long axis of the ellipse. The maximum ellipticity $e = 0.19$ is larger than the THz emission from the plasma filament in the short filament $e = 0.1$ and smaller than that of the long filament $e = 0.48$ [31] and single layer WS_2 with $e = 0.5$ [18]. The ellipticity is determined by the THz relative amplitude of the two orthogonal THz p and s components. The amplitudes of the THz components are dependent on the sample growth structures, such as the thickness along the X axis in Fig. 2(b) and the graphene flake orientation. The ellipticity is also determined by the relative phase difference. These results indicate that the elliptical polarization of THz radiation from VGG can be dynamically controlled via tuning the polarization of the pump beam with the potential for probing the chiral molecular structures, such as protein and DNA [17].

C. THz emission in reflection configuration

We also investigate the helicity-dependent THz emission from VGG in a refection configuration (incident angle $\theta = 45^\circ$) as shown in Fig. 5(a). Similar to the transmission configuration, the peak-valley values of THz p components vary periodically in a $\cos 4\phi$ style with a QWP polarization angle ϕ. The THz peak-valley values of the s components are very sensitive to the photon-helicity states in which the polarity of the THz waveform is reversed for LC and RC polarized excitations. We also fit the experimental data with Eqs. (9) and (10). These fitting values suggest that the contribution from CPDE is nearly the same as that from the transmission configuration, which confirms the reasonable CPDE in the THz radiation mechanism. Moreover, the same THz peak-valley values between transmission and reflection configurations indicate that THz absorption by VGG is almost negligible. THz polarization states in the reflection configuration are shown in Figs. 5(b)–5(d). The results suggest that a linearly polarized pump can introduce almost linearly polarized THz radiation, while a pump with a LC or RC polarization excitation results in a left-handed or right-handed

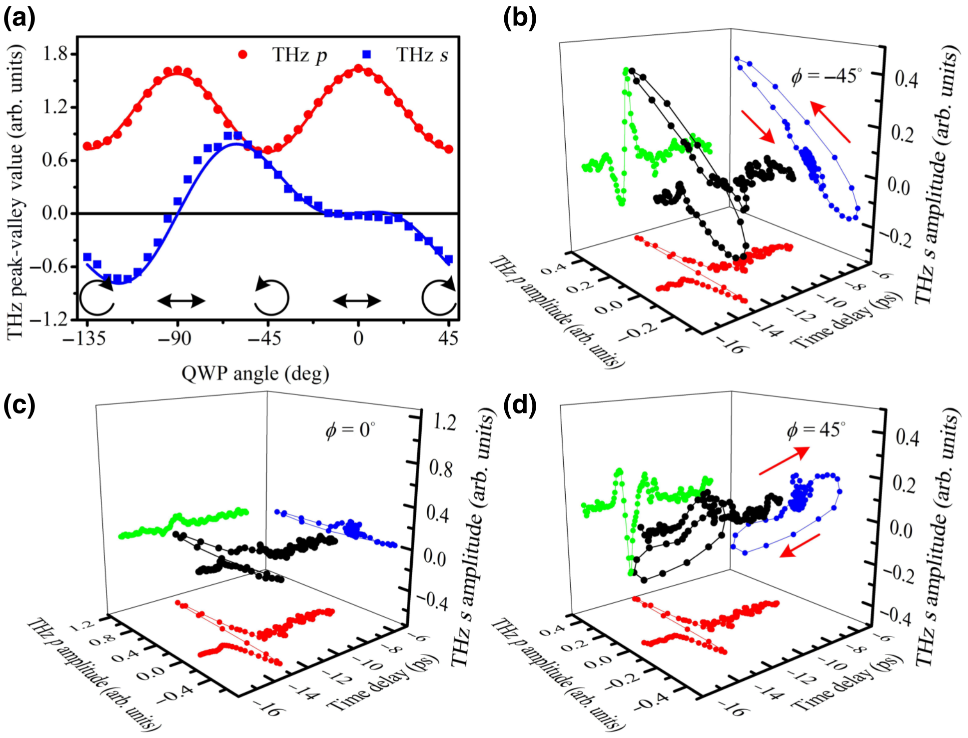

FIG. 5. Helicity-dependent THz emission in a reflection configuration with an incident angle of 45° by tuning the QWP polarization angle. (a) The dependence of the THz peak-valley value on the QWP angle. (b)–(d) show the trajectories of the THz polarization states with QWP angles of −45°, 0°, and 45°, respectively.

elliptical THz pulse, respectively. The same fitting procedures are used for the ellipticity and inclined angle of the ellipse as shown in Fig. 9 and Table III (Appendix F). The helicity direction and ellipticity ($e = 0.18$ for elliptical polarization) of THz waves are same as that of the transmission configuration. The inclined angles of the ellipses are opposite to those in the transmission configuration and they are also dependent on the polarity of THz p and s polarizations. These results also suggest that VGG can be used as a THz emitter with tunable elliptical polarization states by controlling the pump polarization in the reflection configuration as well.

IV. CONCLUSION

To summarize, we experimentally observe the photon-helicity-dependent photocurrent-induced THz emission from VGG. Under the excitation of circular polarized light, the photocarriers in VGG can acquire both transverse momentum and SAM simultaneously due to the LPDE and CPDE. The dependence of THz peak-valley values on the light polarization states can be well fitted by the photon drag effect theory. The fitting parameters can separate the contributions between LPDE and CPDE. Due to the polarization-sensitive photocurrent-induced THz radiation, the THz polarization states can be tuned by varying the pump polarization states. The THz elliptical polarization radiation can be obtained when driven by a circular polarization pump light with the THz helicity direction locked to the helicity of the pump light. THz emission spectroscopy provides an optical method to probe the CPDE in the quantum region and THz emission from VGG has the potential to be an elliptically tunable polarized THz source.

ACKNOWLEDGMENTS

This study was supported by National Natural Science Foundation of China (Grants No. 11774288, No. 11674387, No. 11574368, and No. 11574385), Natural Science Foundation of Shaanxi Province (Grants No. 2019JC-25 and No. 2017KCT-01), International Cooperative Program (Grant No. 201410780) and National Key R&D Program of China (Grants No. 2016YFA0200800 and No. 2016YFA0200400).

APPENDIX A: SYMMETRY POINT GROUP ANALYSIS OF VERTICALLY GROWN GRAPHENE

It is hard to write down the point group of the whole VGG directly from the macroscopic view. However, the analysis can be simplified in a reasonable way as photocurrents generated from graphene flakes in a microscopic view. Instead, we can write down the point group of the graphene flakes from the microscopic view. As shown in Fig. 1(b), graphene flakes are multilayered and their point groups depend on two stacking types, such as the rhombohedral stacking (ABCABC...) described by D_{3d} with an inversion center [24] and Bernal stacking (ABAB...) described by D_{3d} for even layer numbers and D_{3h} for odd layer numbers. If the layer is large enough, the N layer graphene is described by the D_{6h} point group [23,24]. We will discuss the photogalvanic effect and photon drag effect according to the above possible point groups in our samples.

(a) For D_{3h} and D_{6h}, there are 21 fourth-rank tensor elements and the same nonzero elements can be described as

$$\begin{aligned}
&\Phi_{xxxx} = \Phi_{yyyy};\ \Phi_{zzzz}\\
&\Phi_{xxzz} = \Phi_{yyzz};\ \Phi_{xzxz} = \Phi_{yzyz};\ \Phi_{xzzx} = \Phi_{yzzy}\\
&\Phi_{xyxy} = \Phi_{yxyx};\ \Phi_{xxyy} = \Phi_{yyxx};\ \Phi_{xyyx} = \Phi_{yxxy}\\
&\Phi_{zzxx} = \Phi_{zzyy};\ \Phi_{zxzx} = \Phi_{zyzy};\ \Phi_{zxxz} = \Phi_{zyyz}\\
&\Phi_{xxxx} = \Phi_{xxyy} + \Phi_{xyxy} + \Phi_{xyyx}.
\end{aligned} \tag{A1}$$

The fourth-rank tensor-dependent LPDE and CPDE can exist in both D_{3h} and D_{6h}. However, only the D_{3h} point group has four nonzero third-rank tensor elements as follows:

$$\Phi_{yyy} = -\Phi_{yxx} = -\Phi_{xxy} = -\Phi_{xyx}. \tag{A2}$$

TABLE I. PDE and PGE in a graphene system with various stacking orders.

Stacking order	Point group	PDE (fourth-rank tensor)	PGE (third-rank tensor)
Single layer or bulk graphite	D_{6h}	LPDE (D_{6h}) + CPDE (D_{6h})	vanish
ABAB... (rhombohedral stacking)	D_{3d} for even layer numbers	LPDE (D_{3d}) + CPDE (D_{3d}) = LPDE(D_{6h}) + CPDE (D_{6h}) + CPDE′ (D_{3d})	vanish
	D_{3h} for odd layer numbers	LPDE (D_{6h}) + CPDE (D_{6h})	LPGE (D_{3h})
ABCABC... (Bernal stacking)	D_{3d}	LPDE (D_{6h}) + CPDE (D_{6h}) + CPDE′ (D_{3d})	vanish

Thus, the photocurrent density of the LPGE in the D_{3h} point group can be expressed as follows:

$$j_x = -L(E_x E_y^* + E_y E_x^*), \tag{A3}$$

$$j_y = -L(E_x^2 - E_y^2), \tag{A4}$$

where $L = \Phi_{yyy} = -\Phi_{yxx} = (\Phi_{xxy} + \Phi_{xyx})/2$. But the CPGE in D_{3h} vanishes [32]. The LPDE and CPDE in D_{6h} are forbidden as it has an inversion center and the third-rank tensor vanishes.

For the D_{3d} point group, the following 37 fourth-rank tensors are nonzero elements.

$$\begin{array}{l}
\Phi_{xxxx} = \Phi_{yyyy}; \Phi_{zzzz} \\
\Phi_{xxzz} = \Phi_{yyzz}; \Phi_{xzxz} = \Phi_{yzyz}; \Phi_{xzzx} = \Phi_{yzzy} \\
\Phi_{xyxy} = \Phi_{yxyx}; \Phi_{xxyy} = \Phi_{yyxx}; \Phi_{xyyx} = \Phi_{yxxy} \\
\Phi_{zzxx} = \Phi_{zzyy}; \Phi_{zxzx} = \Phi_{zyzy}; \Phi_{zxxz} = \Phi_{zyyz} \\
\Phi_{xxxx} = \Phi_{xxyy} + \Phi_{xyxy} + \Phi_{xyyx} \\
\Phi_{xxxz} = -\Phi_{xyyz} = -\Phi_{yxyz} = -\Phi_{yyxz} \\
\Phi_{xxzx} = -\Phi_{xyzy} = -\Phi_{yxzy} = -\Phi_{yyzx} \\
\Phi_{xzxx} = -\Phi_{xzyy} = -\Phi_{yzxy} = -\Phi_{yzyx} \\
\Phi_{zxxx} = -\Phi_{zxyy} = -\Phi_{zyxy} = -\Phi_{zyyx}
\end{array} . \tag{A5}$$

Compared to the D_{6h} point group, the extra nonzero tensor elements of D_{3d} marked in red just cause the components of the photon drag current as follows:

$$\begin{aligned}
j_x = {} & (\Phi_{xxxz} + \Phi_{xxzx}) q_x \frac{E_x E_z^* + E_z E_x^*}{2} \\
& + (\Phi_{xyyz} + \Phi_{xyzy}) q_y \frac{E_y E_z^* + E_z E_y^*}{2} + \tilde{T}_{xxy} q_x E_y^2 P_{\text{circ}},
\end{aligned} \tag{A6}$$

$$\begin{aligned}
j_y = {} & (\Phi_{yxyz} + \Phi_{yxzy}) q_x \frac{E_y E_z^* + E_z E_y^*}{2} \\
& + (\Phi_{yyxz} + \Phi_{yyzx}) q_y \frac{E_x E_z^* + E_z E_x^*}{2} + \tilde{T}_{yxx} q_x E_x^2 P_{\text{circ}}.
\end{aligned} \tag{A7}$$

When considering the experimental conditions of $q_y = 0$, $E_z = 0$, and E_z^*=0, there are only the last CPDE terms left in Eqs. (A6) and (A7) and the third-rank tensor elements vanish for the D_{3d} point group because the system has an inversion center and PGE is forbidden.

In brief, we summarize the main conclusions in Table I. We can exclude CPGE for the symmetry point group mentioned here. The HRTEM image shows the layer numbers of multilayer graphene flakes are 7–8 layers. Thus, it is more reasonable to analyze the photocurrents based on the symmetry point group of multilayer graphene.

In general, the photocurrent, after considering the above possible symmetry, can be expressed as follows:

$$\begin{aligned}
j_x = {} & T_1 q_x \frac{|E_x|^2 + |E_y|^2}{2} + T_2 q_x \frac{|E_x|^2 - |E_y|^2}{2} \\
& + \tilde{T}_{xxy} q_x E_y^2 P_{\text{circ}} - L(E_x E_y^* + E_y E_x^*),
\end{aligned} \tag{A8}$$

$$\begin{aligned}
j_y = {} & T_2 q_x \frac{E_x E_y{}^* + E_x{}^* E_y}{2} - \tilde{T}_1 q_x P_{\text{circ}} \hat{e}_z (|E_x|^2 + |E_y|^2) \\
& + \tilde{T}_{yxx} q_x E_x^2 P_{\text{circ}} + L(E_y^2 - E_x^2).
\end{aligned} \tag{A9}$$

Here, $\tilde{T}_{xxy}$ and $\tilde{T}_{xxy}$ are pseudotensors of the D_{3d} point group and $L = \Phi_{yyy} = -\Phi_{yxx}$ are the nonlinear tensor elements of the D_{3h} point group.

APPENDIX B: PHOTON-DRAG-EFFECT-INDUCED PHOTOCURRENT IN VERTICALLY GROWN GRAPHENE

Considering the orientation distribution on the substrate surface, we define an orientation angle γ, which is the angle between the Y axis of the laboratory coordinates and the y axis of the crystal coordinates. VGG can be treated as a structure where graphene layers grow vertically on a substrate with the orientation angle of γ as shown in Fig 2(b).

In general, the polarization states can be described by a Jones matrix. When a polarized light E_{in} impinges on a wave plate (WP), the output light from the WP can be described as

$$\begin{aligned}
E_{\text{out}} &= T(-\phi) J(\delta) T(\phi) E_{\text{in}} \\
&= \begin{bmatrix} \cos\phi & -\sin\phi \\ \sin\phi & \cos\phi \end{bmatrix} \begin{bmatrix} 1 & 0 \\ 0 & e^{i\delta} \end{bmatrix} \begin{bmatrix} \cos\phi & \sin\phi \\ -\sin\phi & \cos\phi \end{bmatrix} \begin{bmatrix} E_1 \\ E_2 \end{bmatrix} \\
&= \begin{bmatrix} E_1(\cos^2\phi + \sin^2\phi e^{i\delta}) & E_2(\sin\phi\cos\phi - \sin\phi\cos\phi e^{i\delta}) \\ E_1(\sin\phi\cos\phi - \sin\phi\cos\phi e^{i\delta}) & E_2(\sin^2\phi + \cos^2\phi e^{i\delta}) \end{bmatrix}.
\end{aligned} \tag{B1}$$

Here, $T(\phi)$ is a coordinate rotation matrix and $J(\delta)$ is the Jones matrix for an arbitrary WP with the phase difference δ. In our experiment, the Jones matrix for E_{in} is $\begin{bmatrix} E \\ 0 \end{bmatrix}$ and is $\delta = (\pi/2)$ for a QWP. Thus, we can obtain

$$E_{\text{out}} = E \begin{bmatrix} \cos^2\phi + i\sin^2\phi \\ (1-i)\sin\phi\cos\phi \end{bmatrix}. \tag{B2}$$

The electric vector projection of incident light on the graphene surface in crystal coordinate system *xyz* in Fig. 2(b) can be expressed as

$$\begin{bmatrix} E_x \\ E_y \end{bmatrix} = E \begin{bmatrix} \sin\theta(\cos^2\phi + i\sin^2\phi) \\ \cos\gamma\left(\frac{1}{2} - \frac{i}{2}\right)\sin 2\phi \end{bmatrix}. \tag{B3}$$

The electric vector components in the crystal coordinate system can be expressed as

$$\begin{aligned} |E_x|^2 + |E_y|^2 &= E^2\sin^2\theta(\cos^2\phi + i\sin^2\phi)(\cos^2\phi - i\sin^2\phi) \\ &\quad + \frac{E^2}{4}\{(\cos\gamma\sin 2\phi)(1-i)(\cos\gamma\sin 2\phi)(1+i)\} \\ &= E^2\{\sin^2\theta(3+\cos 4\phi) + \frac{1}{2}\cos^2\gamma\sin^2 2\phi\}, \end{aligned} \tag{B4}$$

$$\begin{aligned} &|E_x|^2 - |E_y|^2 \\ &= E^2\{\sin^2\theta(3+\cos 4\phi) - \frac{1}{2}\cos^2\gamma\sin^2 2\phi\} \end{aligned} \tag{B5}$$

$$\begin{aligned} &E_x{E_y}^* + {E_x}^*E_y \\ &\quad = \frac{1}{2}E^2\cos\gamma\sin\theta\sin 2\phi(\cos^2\phi - sin^2\phi) \\ &\quad = \frac{1}{2}E^2\cos\gamma\sin\theta\sin 4\phi. \end{aligned} \tag{B6}$$

When Eqs. (B4)–(B6) and $q_x = -k\cos\theta$ are substituted into Eqs. (A8) and (A9), the photocurrents in coordinate system *xyz* can be expressed as

$$\begin{aligned} j_x = &-\frac{E^2}{8}k\cos\theta(T_1+T_2)\sin^2\theta\{3+\cos 4\phi\} \\ &-\frac{E^2}{4}k\cos\theta(T_1-T_2)\cos^2\gamma\sin^2 2\phi \\ &-\tilde{T}_{xxy}\frac{1}{2}E^2k\cos\theta\sin^3 2\phi\cos^2\gamma \\ &-LE^2\frac{1}{4}\sin\theta\cos\gamma\sin 4\phi, \end{aligned} \tag{B7}$$

$$\begin{aligned} j_y = &-T_2E^2\frac{1}{8}k\cos\theta\cos\gamma\sin\theta\sin 4\phi \\ &-\tilde{T}_1E^2k\cos\theta\sin\theta\sin 2\phi \\ &\times\left[\frac{1}{4}\sin^2\theta(3+\cos 4\phi) + \frac{1}{2}\cos^2\gamma\sin^2 2\phi\right] \\ &-\tilde{T}_{yxx}k\cos\theta E^2\frac{1}{4}\sin^2\theta(3+\cos 4\phi)\sin 2\phi \\ &-LE^2\left[\frac{1}{4}\sin^2\theta(3+\cos 4\phi) + \frac{1}{2}\cos^2\gamma\sin^2 2\phi\right]. \end{aligned} \tag{B8}$$

The photocurrents in laboratory coordinate system *XYZ* in Fig. 2(b) are

$$\begin{aligned} j_X \propto &-\frac{E^2}{8}k\cos\theta(T_1+T_2)\sin^2\theta\{3+\cos 4\phi\} \\ &-\frac{E^2}{4}k\cos\theta(T_1-T_2)\cos^2\gamma\sin^2 2\phi \\ &-\tilde{T}_{xxy}\frac{1}{2}E^2k\cos\theta\sin^3 2\phi\cos^2\gamma \\ &-LE^2\frac{1}{4}\sin\theta\cos\gamma\sin 4\phi, \end{aligned} \tag{B9}$$

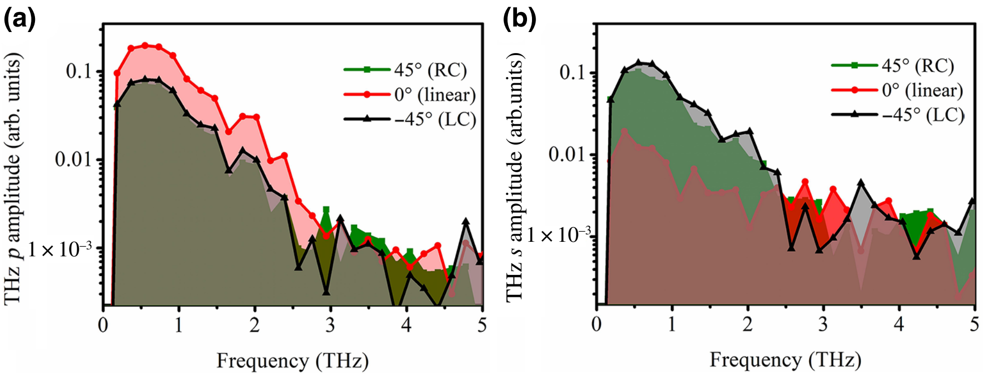

FIG. 6. Frequency-domain spectrum of THz *p* components (a) and *s* components (b) with the excitation of linear, LC, and RC polarization states of the pump beam, respectively.

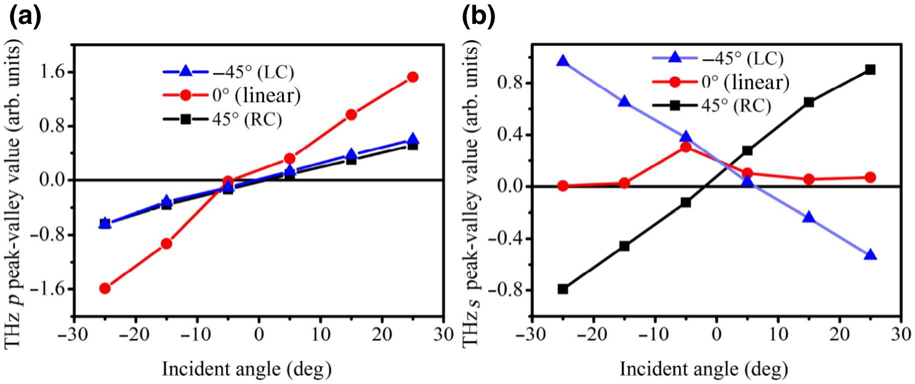

FIG. 7. The incident-angle-dependent peak-valley values of THz p components (a) and THz s components (b) with QWP angles of $-45°$, $0°$, and $45°$ corresponding to the LC, linear and RC polarization states.

$$\begin{aligned} j_Y \propto j_y \cos\gamma \propto & -T_2E^2\frac{1}{8}k\cos\theta\cos^2\gamma\sin\theta\sin 4\phi \\ & -\tilde{T}_1E^2k\cos\theta\sin\theta\sin 2\phi\cos\gamma \\ & \times\left[\frac{1}{4}\sin^2\theta(3+\cos 4\phi)+\frac{1}{2}\cos^2\gamma\sin^2 2\phi\right] \\ & -\tilde{T}_{yxx}k\cos\theta E^2\frac{1}{4}\sin 2\phi\cos\gamma\sin^2\theta(3+\cos 4\phi) \\ & -LE^2\cos\gamma\left[\frac{1}{4}\sin^2\theta(3+\cos 4\phi)+\frac{1}{2}\cos^3\gamma\sin^2 2\phi\right], \end{aligned} \tag{B10}$$

$$\begin{aligned} j_Z \propto j_y\sin\gamma \propto & -T_2E^2\frac{1}{8}k\cos\theta\frac{1}{2}\sin 2\gamma\sin\theta\sin 4\phi \\ & -\tilde{T}_1E^2k\cos\theta\sin\theta\sin 2\phi\sin\gamma \\ & \times\left[\frac{1}{4}\sin^2\theta(3+\cos 4\phi)+\frac{1}{2}\cos^2\gamma\sin^2 2\phi\right] \\ & -\tilde{T}_{yxx}k\cos\theta E^2\frac{1}{4}\sin^2\theta\sin\gamma(3+\cos 4\phi)\sin 2\phi \\ & -LE^2\sin\gamma\left[\frac{1}{4}\sin^2\theta(3+\cos 4\phi)+\frac{1}{2}\cos^2\gamma\sin^2 2\phi\right]. \end{aligned} \tag{B11}$$

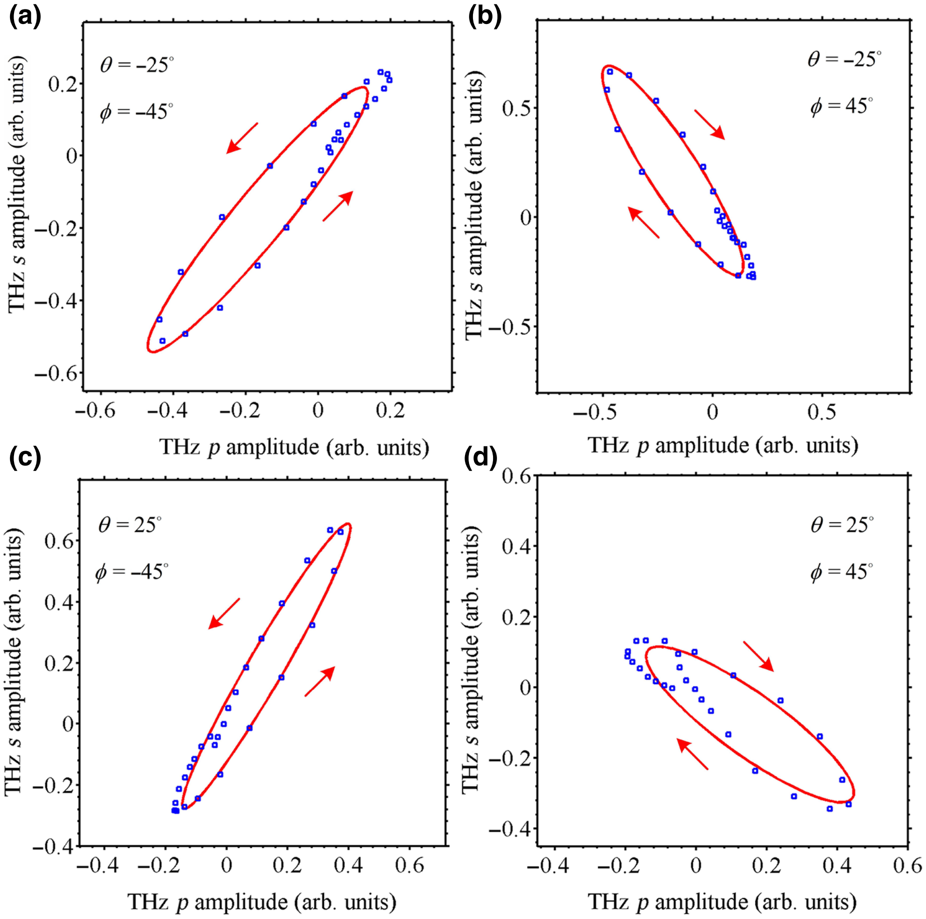

FIG. 8. Fitting results of THz polarization states in a transmission configuration with the incident angle of $\theta = \pm 25°$ and QWP angle $\phi = \pm 45°$. The blue dots are experimental data and the red solid lines are fitting results based on least-squares method. The red arrows mark the helix direction.

TABLE II. Fitting parameters of elliptical THz polarization state in a transmission configuration.

Incident angle (degrees)	QWP angle (degrees)	Long axis	Short axis	Ellipticity	Inclined angle (degrees)	Helicity direction
−25	−45 (LC)	1.1273	0.2293	0.2034	−57.2403	left-handed
	45 (RC)	0.9407	0.1428	0.1518	50.6077	right-handed
25	−45 (LC)	0.7157	0.1763	0.2463	−35.7331	left-handed
	45 (RC)	1.0786	0.1181	0.1095	59.7742	right-handed

In order to satisfy the experimental condition $j_Y(\phi = 45^\circ) = -j_Y(\phi = -45^\circ)$ as shown in Fig. 3(b), the last L related terms must vanish. Thus, we can exclude the LPGE terms caused by the D_{3h} point group because the LPGE terms do not change the polarity with the helicity of the pump beam. Then all the terms of the photocurrents are caused by the D_{3d} symmetry point group and this includes all the photocurrent terms from the D_{6h} point group. According to dipole radiation theory, the s and p polarization components of a photocurrent-induced THz wave can be expressed as

$$\begin{aligned} E^p_{\rm THz} &\propto t_p\left(\sin\theta_{\rm in}\frac{\partial j_X}{\partial t} + cos\theta_{\rm in}\frac{\partial j_Z}{\partial t}\right) \\ &\propto L_1\cos 4\phi + Msin^2 2\phi + C_1\sin 2\phi\cos 4\phi \\ &\quad + C_2\sin 2\phi + C_3 sin^3 2\phi + D, \end{aligned} \tag{B12}$$

$$\begin{aligned} E^s_{\rm THz} &\propto t_s\frac{\partial j_Y}{\partial t} \propto L_2\sin 4\phi + C_4\sin 2\phi \\ &\quad + C_5\sin 2\phi\cos 4\phi + C_6\sin^2 2\phi, \end{aligned} \tag{B13}$$

where $\sin\theta_{in} = (\sqrt{\varepsilon_2}/\sqrt{\varepsilon_1})\sin\theta_{\rm det}$, $\theta_{\rm in}$ is the radiation angle inside the medium, and $\theta_{\rm det}$ is the detection angle, which is the reflection angle or transmission angle for either the reflection or transmission configuration. The coefficients L_1 and L_2 are related to $T_1 + T_2$ and T_2. C_1 and C_2 are related to $\tilde{T}_1 + \tilde{T}_{yxx}$. C_3, C_4, C_5, and C_6 are related to $\tilde{T}_{xxy}$, $\tilde{T}_1 + \tilde{T}_{yxx}$, $\tilde{T}_1 + \tilde{T}_{yxx}$, and $\tilde{T}_1$, respectively. M is related to $\tilde{T}_1$ and $T_1 + T_2$. D is a constant and is related to $T_1 + T_2$.

APPENDIX C: FOURIER TRANSFORMATION OF THZ TIME-DOMAIN SIGNAL AT DIFFERENT PUMP POLARIZATIONS

The frequency spectra of the emitted THz signals can be acquired by fast Fourier transformation. Figures 6(a) and 6(b) show the frequency spectra of THz p and s components with the polarization states of the excitation beam at linear, LC and RC polarization.

APPENDIX D: THE DEPENDENCE OF THZ PEAK-VALLEY VALUES ON INCIDENT ANGLES

The THz amplitude should be affected by different incident angles because the mechanism of THz emission from VGG is based on wave-vector-dependent PDE. Figures 7(a) and 7(b) show the incident-angle-dependent peak-valley value of THz p and THz s components with the polarization states of the excitation beam at linear, LC and RC polarization.

APPENDIX E: FITTING OF ELLIPTICAL THZ POLARIZATION STATES IN A TRANSMISSION CONFIGURATION

To acquire the elliptical THz polarization states, we have fitted experimental data in a transmission configuration using an ellipse function based on the least squares method

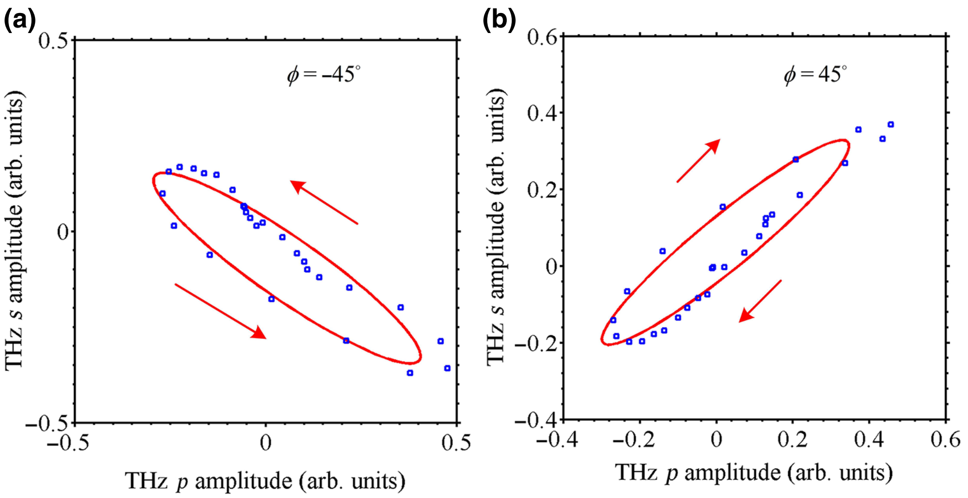

FIG. 9. Fitting results of THz elliptical polarization states driven by LC ($\phi = -45^\circ$) and RC ($\phi = 45^\circ$) polarized light in a reflection configuration based on least-squares method.

TABLE III. Fitting parameters of elliptical THz polarization state in a reflection configuration.

QWP angle (degrees)	Long axis	Short axis	Ellipticity	Inclined angle (degrees)	Helicity direction
−45 (LC)	0.8279	0.1376	0.1662	39.2651	left-handed
45 (RC)	0.8438	0.1612	0.1911	−34.6694	right-handed

[13] as shown in Fig. 8. The related ellipse parameters are listed in Table II.

APPENDIX F: FITTING OF ELLIPTICAL THZ POLARIZATION STATES IN A REFLECTION CONFIGURATION

The same ellipse fitting process has been made to the experimental data in a reflection configuration as shown in Fig. 9 and the ellipse parameters have been listed in Table III.

[1] R. A. Beth, Mechanical detection and measurement of the angular momentum of light, Phys. Rev. **50**, 115 (1936).

[2] V. A. Shalygin, H. Diehl, C. Hoffmann, S. N. Danilov, T. Herrle, S. A. Tarasenko, D. Schuh, C. Gerl, W. Wegscheider, W. Prettl, and S. D. Ganichev, Spin photocurrents and the circular photon drag effect in (110)-grown quantum well structures, JETP Lett. **84**, 570 (2007).

[3] J. Karch, P. Olbrich, M. Schmalzbauer, C. Zoth, C. Brinsteiner, M. Fehrenbacher, U. Wurstbauer, M. M. Glazov, S. A. Tarasenko, E. L. Ivchenko, D. Weiss, J. Eroms, R. Yakimova, S. Lara-Avila, S. Kubatkin, and S. D. Ganichev, Dynamic Hall Effect Driven by Circularly Polarized Light in a Graphene Layer, Phys. Rev. Lett. **105**, 227402 (2010).

[4] S. D. Ganichev, E. L. Ivchenko, and W. Prettl, Photogalvanic effects in quantum wells, Phys. E **14**, 166 (2002).

[5] S. D. Ganichev, E. L. Ivchenko, V. V. Bel'kov, S. A. Tarasenko, M. Sollinger, D. Weiss, W. Wegscheider, and W. Prettl, Spin-galvanic effect, Nature **417**, 153 (2002).

[6] V. A. Shalygin, M. D. Moldavskaya, S. N. Danilov, I. I. Farbshtein, and L. E. Golub, Circular photon drag effect in bulk tellurium, Phys. Rev. B **93**, 045207 (2016).

[7] L. Prechtel, L. Song, D. Schuh, P. Ajayan, W. Wegscheider, and A. W. Holleitner, Time-resolved ultrafast photocurrents and terahertz generation in freely suspended graphene, Nat. Commun. **3**, 646 (2012).

[8] D. Sun, C. Divin, J. Rioux, J. E. Sipe, C. Berger, W. A. de Heer, P. N. First, and T. B. Norris, Coherent control of ballistic photocurrents in multilayer epitaxial graphene using quantum interference, Nano Lett. **10**, 1293 (2010).

[9] L. Braun, G. Mussler, A. Hruban, M. Konczykowski, T. Schumann, M. Wolf, M. Munzenberg, L. Perfetti, and T. Kampfrath, Ultrafast photocurrents at the surface of the three-dimensional topological insulator Bi_2Se_3, Nat. Commun. **7**, 13259 (2016).

[10] S. Y. Hamh, S.-H. Park, S.-K. Jerng, J. H. Jeon, S.-H. Chun, and J. S. Lee, Helicity-dependent photocurrent in a Bi_2Se_3 thin film probed by terahertz emission spectroscopy, Phys. Rev. B **94**, 161405 (2016).

[11] Y. Huang, Z. Yao, C. He, L. Zhu, L. Zhang, J. Bai, and X. Xu, Terahertz surface and interface emission spectroscopy for advanced materials, J. Phys.: Condens. Matter **31**, 153001 (2019).

[12] P. A. Obraztsov, T. Kaplas, S. V. Garnov, M. Kuwata-Gonokami, A. N. Obraztsov, and Y. P. Svirko, All-optical control of ultrafast photocurrents in unbiased graphene, Sci. Rep. **4**, 4007 (2014).

[13] P. A. Obraztsov, N. Kanda, K. Konishi, M. Kuwata-Gonokami, S. V. Garnov, A. N. Obraztsov, and Y. P. Svirko, Photon-drag-induced terahertz emission from graphene, Phys. Rev. B **90**, 241416 (2014).

[14] J. Maysonnave, S. Huppert, F. Wang, S. Maero, C. Berger, W. de Heer, T. B. Norris, L. A. De Vaulchier, S. Dhillon, J. Tignon, R. Ferreira, and J. Mangeney, Terahertz generation by dynamical photon drag effect in graphene excited by femtosecond optical pulses, Nano Lett. **14**, 5797 (2014).

[15] Y.-M. Bahk, G. Ramakrishnan, J. Choi, H. Song, G. Choi, Y. H. Kim, K. J. Ahn, D.-S. Kim, and P. C. Planken, Plasmon enhanced terahertz emission from single layer graphene, ACS Nano **8**, 9089 (2014).

[16] L. Zhu, Y. Huang, Z. Yao, B. Quan, L. Zhang, J. Li, C. Gu, X. Xu, and Z. Ren, Enhanced polarization-sensitive terahertz emission from vertically grown graphene by a dynamical photon drag effect, Nanoscale **9**, 10301 (2017).

[17] X. Lu and X. C. Zhang, Generation of Elliptically Polarized Terahertz Waves from Laser-Induced Plasma with Double Helix Electrodes, Phys. Rev. Lett. **108**, 123903 (2012).

[18] L. Zhang, Y. Huang, L. Zhu, Z. Yao, Q. Zhao, W. Du, Y. He, and X. Xu, Polarized THz emission from in-plane dipoles in monolayer tungsten disulfide by linear and circular optical rectification, Adv. Opt. Mater. **7**, 1801314 (2019).

[19] Z. H. Ni, H. M. Fan, Y. P. Feng, Z. X. Shen, B. J. Yang, and Y. H. Wu, Raman spectroscopic investigation of carbon nanowalls, J. Chem. Phys. **124**, 204703 (2006).

[20] X. C. Zhang and D. H. Auston, Optoelectronic measurement of semiconductor surfaces and interfaces with femtosecond optics, J. Appl. Phys. **71**, 326 (1992).

[21] R. W. Boyd, *Nonlinear Optics*, 3rd ed. (Academic Press, Orlando, 2008).

[22] J. Karch, P. Olbrich, M. Schmalzbauer, C. Brinsteiner, U. Wurstbauer, M. Glazov, S. Tarasenko, E. Ivchenko, D. Weiss, and J. Eroms, Photon helicity driven electric currents in graphene, arXiv preprint arXiv:1002.1047 (2010).

[23] L. M. Malard, M. H. D. Guimarães, D. L. Mafra, M. S. C. Mazzoni, and A. Jorio, Group-theory analysis of electrons and phonons in *N*-layer graphene systems, Phys. Rev. B **79**, 125426 (2009).

[24] J. L. Mañes, F. Guinea, and M. A. H. Vozmediano, Existence and topological stability of Fermi points in multilayered graphene, Phys. Rev. B **75**, 155424 (2007).

[25] C.-M. Tu, Y.-C. Chen, P. Huang, P.-Y. Chuang, M.-Y. Lin, C.-M. Cheng, J.-Y. Lin, J.-Y. Juang, K.-H. Wu, J.-C. A. Huang, W.-F. Pong, T. Kobayashi, and C.-W. Luo, Helicity-dependent terahertz emission spectroscopy of topological insulator Sb_2Te_3 thin films, Phys. Rev. B **96**, 195407 (2017).

[26] C. Jiang, V. A. Shalygin, V. Y. Panevin, S. N. Danilov, M. M. Glazov, R. Yakimova, S. Lara-Avila, S. Kubatkin, and S. D. Ganichev, Helicity-dependent photocurrents in graphene layers excited by midinfrared radiation of a CO_2 laser, Phys. Rev. B **84**, 125429 (2011).

[27] P. Olbrich, C. Drexler, L. E. Golub, S. N. Danilov, V. A. Shalygin, R. Yakimova, S. Lara-Avila, S. Kubatkin, B. Redlich, R. Huber, and S. D. Ganichev, Reststrahl band-assisted photocurrents in epitaxial graphene layers, Phys. Rev. B **88**, 245425 (2013).

[28] M. M. Glazov and S. D. Ganichev, High frequency electric field induced nonlinear effects in graphene, Phys. Rep. **535**, 101 (2014).

[29] M. V. Entin, L. I. Magarill, and D. L. Shepelyansky, Theory of resonant photon drag in monolayer graphene, Phys. Rev. B **81**, 165441 (2010).

[30] A. Fitzgibbon, M. Pilu, and R. B. Fisher, Direct least square fitting of ellipses, IEEE Trans. Pattern Anal. Mach. Intell. **21**, 476 (1999).

[31] Z. Zhang, Y. Chen, S. Cui, F. He, M. Chen, Z. Zhang, J. Yu, L. Chen, Z. Sheng, and J. Zhang, Manipulation of polarizations for broadband terahertz waves emitted from laser plasma filaments, Nat. Photonics **12**, 554 (2018).

[32] B. I. Sturman and V. M. Fridkin, *The Photovoltaic and Photorefractive Effects in Noncentrosymmetric Materials* (Gordon and Breach Science Publishers, Philadelphia, 1992).